PCCP

Accepted Manuscript

ROYAL SOCIETY OF CHEMISTRY

www.rsc.org/pccp

Ligand-assisted Soft-Chemical Synthesis of Self-assembled Shaped Mesoporous Co_3O_4: Efficient Visible Light Photocatalyst

Mouni Roy, Sourav Ghosh, and Milan Kanti Naskar*

Sol-Gel Division, CSIR-Central Glass and Ceramic Research Institute, Kolkata 700 032, India

Abstract: Mesoporous self-assembled cobalt oxide (Co_3O_4) of different shapes was synthesized by a facile soft-chemical process using cobalt nitrate, oxalic acid and phosphoric acid in the presence of cationic templates, cetyltrimethylammonium bromide, 1-butyl-3-methylimidazolium bromide, and pyridinium bromide at 75^{o}C/2h followed by calcination at 300^{o}C. The effect of cationic templates of the samples on the physico-chemical properties, and the photocatalytic efficiency for the degradation of Chicago Sky Blue 6B was studied. Pyridinium bromide and 1-butyl-3-methylimidazolium bromide facilitated shaped morphology formation compared to cetyltrimethylammonium bromide. The rod-like particles having higher surface area exhibited higher photocatalytic performance.

*Corresponding author. E-mail: milan@cgcri.res.in, Fax: +91 33 24730957

1. Introduction

With the advancement of nanotechnology, controllable and selective synthesis of nanomaterials have attracted intense research interest due to their unique physical and chemical properties, which are significantly different from those of bulk materials.[1,2] Morphological tuning of the materials is important because it influences in different

properties of the materials. Mesoporous nanomaterials with tuned morphology, in particular are becoming more important for potential applications in catalysis, sensors, fuel cells, supercapacitors etc.[3,4]

Among the transition metal oxides, nanostructured tricobalt tetraoxide (Co_3O_4), a p-type semiconductor, finds widespread applications in chemical sensor,[5] lithium-ion batteries,[6] optical and magnetic materials,[7,8] and heterogeneous catalysts,[9] where their properties are strongly dependent on their size and shape.[10] The band gap of the semiconductor lies in the range of 1.9-2.0 eV. Thus it is capable of forming electron – hole pair on irradiation by visible light. In recent years, Co_3O_4 with various morphologies such as nanorods,[11] nanowires,[12] nanotubes,[13] nanobelts,[14] nanocubes,[15] nanosheets[16-18] etc. have been synthesized successfully. Chen *et al.*[19] prepared various cobalt-based nanostructured materials (nanocubes, nanodiscs and nanoflowers) by hydrothermal method. These Co_3O_4 nanostructures have superior properties to their bulk counterparts in terms of heterogeneous catalysts for NO_x reduction, CO oxidation[20] and VOC removal[21] etc.

Visible light covers the largest ratio of the solar spectrum. Thus involvement of easily available, naturally gifted visible light in finding an alternative to energy and environmental issues is a topic of immense research interests.[22] Suitable designing of photocatalyst has been focused to perform photocatalytic water splitting or degradation of water soluble organic pollutants under visible light irradiation. Efforts are given not only to improve catalytic efficiency of TiO_2[23] but also to synthesize other less costly visible-light-driven semiconductor composites[24-26] and pure transition metal oxides[27] catalyst.

The photocatalytic role of Co_3O_4 has been reported by many researchers.[28-31] Warang *et al.* showed the photocatalytic efficiency of Co_3O_4 for degradation of methylene blue via Photo-Fenton reaction.[28] Photocatalytic degradation of methyl violet in the presence of Co_3O_4 catalyst has been reported by Li *et al.*[29] Lou *et al.* synthesized Co_3O_4 nanorods, and studied photocatalytic degradation of different active dyes.[30] In a recent time, Pan *et al.* have shown the photocatalytic performance of Co_3O_4 nanostructured materials for the degradation of methyl orange.[31]

Mesoporous Co_3O_4 with higher surface area enhances the adsorption and diffusion of reactant molecules toward better catalytic performance of the oxides. Mesoporous Co_3O_4 is generally synthesized by either hard templating route using KIT-6, SBA-15 and SBA-16 silica,[32,33] and carbon spheres[34] as hard templates or soft templating process[35] using Pluronic block copolymer as soft templating agent. Hard templating route is an effective method to prepare mesoporous metal oxides. However, hard templating method is tedious involving multi-steps reaction pathway for the removal of hard templates, use of harmful hydrofluoric acid or sodium hydroxide etc. Therefore, development of a simple, environmental benign method is important for the synthesis of mesoporous transition metal oxides. Zheng *et al.*[36] synthesized flower-like mesoporous Co_3O_4 by solvothermal method. Mesoporous Co_3O_4 microcubes were synthesized by solvothermal method using diethylene glycol (DEG) as organic solvent.[37] Wang *et al.*[38] synthesized porous Co_3O_4 nanowires by annealing as-prepared cobalt-carbonate-hydroxide by hydrothermal method. Zhu *et al.* reported solvothermal approach for the shape-controlled synthesis of porous Co_3O_4 following thermal decomposition of the corresponding cobalt carbonate/hydroxide intermediates.[39] Metal carboxylates are

effective precursors for the synthesis of metal oxides in terms of low cost, easy synthesis process etc. Using reverse micelles process, copper oxalate nanorods with tuned size and morphology were prepared by Ranjan *et al*.[40] Guo *et al.* synthesized various transition metal oxides with high crystallinity by thermal decomposition of corresponding transition metal oxalate.[41] We report for the synthesis of mesoporous CuO with multi-shell patterned structures obtained from the thermal decomposition of copper oxalate.[42] Using organic solvents like N,N-dimethylacetamide (DMA) and dimethyl sulphoxide (DMSO), Wang *et al* synthesized cobalt oxalate and mesoporous Co_3O_4 nanostructures.[43] Nanostructured Co_3O_4 was obtained via thermal decomposition of nanostructured cobalt oxalate precursor synthesized through microemulsion-mediated technique[44,45] and via surfactant-free soft chemical precipitation process.[46]

Ionic liquids (ILs) are a class of low temperature molten salts composed of organic cations and inorganic or organic anions with high polarity and a preorganized solvent structure. They have little measurable vapour pressure, high thermal stability, and tunable solubilities for inorganic and organic molecules. Due to their unique properties, they have been used as solvent, additives, templates, or precursors in designing materials synthesis.[47] Ionic liquids have been exploited for the synthesis of zeolites, inorganic-organic hybrid materials,[48] mesoporous silica[49]etc. Wang *et al.* reported the synthesis of ionic liquid (1-buty-3-methylimidazolium iodide) modified BiOI which showed superior photocatalytic activity to the unmodified BiOI.[50] Microwave-assisted synthesis of cobalt oxalate nanorods in the presence of ionic liquid followed by their thermal conversion to Co_3O_4 rods was reported by Wang and Zhu.[51]

Keeping the above views in mind, the objective of the present investigation is to study the role of different cationic templates toward the formation of self-assembled shaped mesoporous Co_3O_4 via a simple soft chemical, ligand-assisted process using cobalt nitrate, oxalic acid, and phosphoric acid at 75^oC/2h followed by calcinations at 300^oC. In this work, the effect of ILs, pyridinium bromide (PB) and 1-butyl-3-methylimidazolium bromide (IB), and cetyltrimethylammonium bromide (CTAB) as templates on the physico-chemical behaviors of Co_3O_4 was studied. The structure of CTAB, 1-butyl-3-methylimidazolium bromide, and pyridinium bromide are shown in Fig. S1 (ESI). The photocatalytic performance of the synthesized products was evaluated and illustrated in terms of morphology and textural properties. Chicago Sky Blue 6B (CSB) (chemical structure is shown in Fig. S1, ESI), a carcinogenic azo dye widely used in the textile, paper, food and pharmaceutical industries[52] was degraded using the Co_3O_4 catalysts. This study provides new insights into the design and synthesis of other transition metal oxides for their various applications. To the best of our knowledge, we are the first to report the effect of cationic templates (CTAB and IL: PB and IB) on the morphology and textural property of designed mesoporous Co_3O_4 shaped particles, and their dual influence on the rapid visible-light-driven photocatalysis by synthesised pure Co_3O_4 catalysts.

2. EXPERIMENTAL SECTION

Synthesis. Cetyltrimethylammonium bromide (CTAB), 1-butyl-3-methylimidazolium bromide (IB), and pyridinium bromide (PB) were purchased from Sigma-Aldrich. Cobalt

nitrate hexahydrate ($Co(NO_3)_3.6H_2O$, oxalic acid and phosphoric acid were from Merck, India. Deionized (DI) water was used throughout the experiment.

In a typical experiment, 20 mmol cobalt nitrate hexahydrate was dissolved in 140 mL of water followed by adding different amount of cationic templates, CTAB, pyridinium bromide and 1-butyl-3-methylimidazolium bromide, maintaining the molar ratio of template : $Co(NO_3)_2.6H_2O$ as 0.2, 0.3 and 0.4 each. The mix solution was stirred vigorously at 75^oC for 2h. A total of 60 mL of 12 mmol oxalic acid solution in water containing 2 mL phosphoric acid was slowly added into the former solution under vigorous stirring at 75^oC. The molar ratio of $Co(NO_3)_2.6H_2O$: oxalic acid was maintained as 1:0.6. The stirring was continued for 5 mins to obtain a pink viscous mass. The hot viscous material was quenched in ice-water followed by centrifugation (6000 rpm) and washing (thrice) with acetone. It was then dried at 60^oC for 24 h followed by calcinations at 300 ^oC for 2h at the heating rate of 1 ^{o} C/min. The samples were designated as CTAB-0.2, CTAB-0.3, CTAB-0.4, IB-0.2, IB-0.3, IB-0.4, PB-0.2, PB-0.3, PB-0.4 for 0.2, 0.3 and 0.4 molar ratio of the templates : Co^{2+}, respectively using CTAB, IB and PB.

Characterization. The thermal behaviours of the uncalcined (as-prepared) particles were studied by thermogravimetry (TG) and differential thermal analysis (DTA) with (Netzsch STA 449C, Germany) from room temperature to 600^oC in air atmosphere at the heating rate of 10^oC/min. X-ray diffraction (XRD) studies of the calcined powders were performed by Philips X'Pert Pro PW 3050/60 powder diffractometer using Ni-filtered Cu-K_α radiation (λ = 0.15418 nm) operated at 40 kV and 30 mA. The characteristic vibration bands of the products were confirmed by FTIR (Nicolet 5PC, Nicolet Analytical Instruments, Madison, WI) with KBr pellet at a resolution of 4 cm^{-1}. The

Raman spectrum was recorded with a RENISHAW spectrometer with 514 nm radiation from an argon laser at room temperature. Nitrogen adsorption-desorption measurements were conducted at 77 K with a Quantachrome (ASIQ MP) instrument. The samples were outgassed in vacuum at 250^{o}C for 4 h prior to the measurement. The surface area was obtained using Brunauer-Emmet-Teller (BET) method within the relative pressure (P/P_o) range of 0.05-0.20 and the pore size distribution was calculated by Barret-Joyner-Halenda (BJH) method. The nitrogen adsorption volume at the relative pressure (P/P_o) of 0.99 was used to determine the pore volume. The morphology of the particles was examined by field emission scanning electron microscopy, FESEM with Zeiss, Supra^{TM} 35VP instrument operating with an accelerating voltage of 10 kV, and transmission electron microscopy, TEM using a Tecnai G2 30ST (FEI) instrument operating at 300 kV. The UV visible spectra were recorded using UV-visible-NIR spectrophotometer (UV – 3101PC, Shimadzu).

Photocatalytic test. In a typical photocatalytic test, 20 mg of the prepared Co_3O_4 sample was mixed with 60 mL of 10^{-5} M Chicago Sky Blue 6B (CSB) dye solution followed by stirring for about 30 minutes in dark for homogenization. Aliquots were taken out, filtered by Millipore filter paper (pore dia 0.22 μm). The filtrates were analyzed using a UV-visible spectrophotometer. Rest of the dye solution was placed in a rectangular box (68 cm x 25 cm x 36 cm). At the inside top of the box two tubes, each with a power of 18 W, are attached. The solution was irradiated from a distance of 11 cm by visible light (λ= 465 nm) at room temperature in the photoreactor. After a time interval of 3 minutes of irradiation, aliquots were collected, filtered and monitored by UV-visible

spectrophotometer. The decrease in absorption intensity at λ_{max}=618 nm indicates the photocatalytic degradation of the organic dye.

3. RESULTS AND DISCUSSION

Ligand-assisted Shaped Mesoporous Co_3O_4. Figure 1A shows the XRD patterns of the as-prepared samples synthesized at 75^{o}C/2h using different templates, (a) CTAB, (b) IB and (c) PB with molar ratio of template : Co^{2+} as 0.3. It confirms the characteristic peaks of hydrated cobalt oxalate which can be indexed to the orthorhombic phase of $CoC_2O_4.xH_2O$ (JCPDS No. 25-0250). After calcination at 300^{o}C, cubic Co_3O_4 phase (JCPDS File No. 43-1003) was formed for the corresponding samples (Fig. 1B). It is to be noted that the presence of Co^{2+} in the as-prepared $CoC_2O_4.xH_2O$ is octahedrally coordinated,[53] and it is metastable form. The Co_3O_4 has a spinel structure containing Co^{3+} in an octahedral coordination and Co^{2+} in a tetrahedral coordination,[54] which is thermodynamically stable. Therefore, calcination of the as-prepared $CoC_2O_4.xH_2O$ in air atmosphere, the thermodynamically stable Co_3O_4 spinel was formed. By changing the molar concentration ratio of templates : Co^{2+} to 0.2 and 0.4, the crystallization behaviours remain unchanged for both the (A) as-prepared and (B) calcined samples as evidenced from their XRD peak positions (Figs. S2 (a) CTAB-0.2, (b) IB-0.2, (c) PB-0.2, and S3 (a) CTAB-0.4, (b) IB-0.4, (c) PB-0.4, ESI).

The DTA and TG analysis of the as-prepared (uncalcined) samples prepared using (A) CTAB, (B) IB (C) PB with molar ratio of template : Co^{2+} = 0.3 each is shown in Fig. S4 (ESI). In TG analysis, it is observed that significant mass loss occurred in two distinct steps i.e, up to 200^{o}C and 200^o-300^{o}C. The curves shows the endothermic peaks at

around 165°-170°C, accompanying with sharp mass loss of 19% and 15% using CTAB and IB, and PB, respectively, up to 200°C in TG curve. The DTA curves exhibit the exothermic peaks at around 265°-270°C with a sharp mass loss of about 37% in the temperature range 200°-300°C. The endothermic peaks of the samples attributed to the removal of structural water corresponding to the first step mass loss of 15%-19%. The exothermic peak was due to decomposition of cobalt oxalate revealing the second step mass loss of about 37%. A small fraction of mass loss (2-4%) occurred from 300°-600°C which could be due to the removal of residual amount of templates entrapped in the samples. Based on the thermal analysis, the total decomposition process can be expressed as:

$$CoC_2O_4.xH_2O \rightarrow CoC_2O_4 + xH_2O \quad (1)$$

$$3CoC_2O_4 + 2O_2 \rightarrow Co_3O_4 + 6CO_2 \quad (2)$$

The FTIR spectra of the as-prepared samples synthesized using CTAB, IB and PB with molar ratio of template : Co^{2+} as 0.3 are shown in Fig. 2A, while Fig. 2B reveal the FTIR spectra of the corresponding calcined samples. For the as-prepared samples (Fig. 2A), the absorption band at around 3358 cm^{-1} is assigned to the water of hydration. The strong peak at 1627 cm^{-1} is attributed to the C=O stretching vibration, while the absorption bands at 1363 cm^{-1} and 1315 cm^{-1} are ascribed to C-O asymmetric and symmetric vibrations, respectively. It indicates the presence of bridging oxalates with all four oxygen atoms coordinated to the metal atoms.[55] The asymmetric O-C-O band appears at 833 cm^{-1}, and symmetric C-C-O band is found at 487 cm^{-1}. However, for the calcined samples (Fig. 2B), two sharp absorption bands are noticed at 565 cm^{-1} and 667

cm^{-1}, which corresponded to spinel Co-O stretching vibration mode,[56] the former peak was assigned to octahedrally co-ordinated Co^{3+}, while the latter was due to tetrahedrally co-ordinated Co^{2+}. By changing the molar concentration ratio of templates : Co^{2+} to 0.2 and 0.4, the FTIR peak positions remain unchanged for both the (A) as-prepared and (B) calcined samples (Figs. S5 (a) CTAB-0.2, (b) IB-0.2, (c) PB-0.2, and S6 (a) CTAB-0.4, (b) IB-0.4, (c) PB-0.4, ESI).

Raman spectra of as-prepared $CoC_2O_4.xH_2O$ prepared using CTAB, IB, PB with molar ratio of template : Co^{2+} as 0.3 is shown in Fig. 3A. For CTAB-templated samples, the stronger bands at 1470 cm^{-1} with a shoulder at 1447 cm^{-1} along with other bands at 917 cm^{-1}, 589 cm^{-1}, 531 cm^{-1} corroborated with the presence of cobalt oxalate.[57] Interestingly, in the presence of pyridinium bromide (PB), each Raman peak shifted a little extent to lower wavenumbers, while a significant shifting of the corresponding peaks to 1455 cm^{-1}, 1434 cm^{-1}, 896 cm^{-1}, 572 cm^{-1}, 511 cm^{-1} for 1-butyl-3-methylimidazolium bromide (IB)-templated samples is noticed. Due to more delocalization of π-electron[58] in 1-butyl-3-methylimidazolium bromide compared to pyridinium bromide, the Raman peaks of the former sample shifted toward lower wavenumber compared to those in latter sample. For the calcined samples prepared in the presence of CTAB, the characteristic bands at 195 cm^{-1}, 522 cm^{-1} and 618 cm^{-1} were attributed to the F_{2g} Raman active modes, and those appeared at 481 cm^{-1} and 688 cm^{-1} were due to E_g and A_{1g} modes, respectively (Fig. 3B). The Raman mode A_{1g} corresponded to the characteristics of octahedral sites, and E_g and F_{2g} modes were assigned to the combined vibrations of tetrahedral site and octahedral oxygen motions.[59] The peak shifting toward lower wavenumber for 1-butyl-3-methylimidazolium bromide-

templated sample is also noticed in calcined samples. From thermal analysis (Fig. S4A-C), it is clear that a little amount of template remained undecomposed even after calcinations at 300^{o}C, which could contribute for peak shifting due to the presence of more delocalized π-electron in 1-butyl-3-methylimidazolium bromide as observed in the case of as-prepared samples.

Figure 4a-c shows the FESEM microstructures of the calcined (300^{o}C) samples prepared using (a) CTAB, (b) IB and (c) PB with molar ratio of template : Co^{2+} = 0.2. It is clear that flake-like particles were obtained using CTAB, while IB and PB rendered dice-like particles in which the smaller particles self-assembled in a proper alignment. The higher magnification images of corresponding microstructures are shown in Fig. S7a-c (ESI). Interestingly, with increase in molar ratio of template : Co^{2+} to 0.3, the flake-like particles of CTAB-assisted samples transformed to a mixture of dice and rod-like particles (Fig. 4d). From the higher magnified FESEM image (S7d (ESI)), it is seen that the dice-like particles comes in vicinity to each other, dissolute and join forming nut-bolt-like shape (marked with rectangle). With increasing the concentration of the CTAB, more and more template molecules adsorb onto the surface of the crystals via hydrogen bonding and van der Waals force, thus favouring nut-bolt-like shape. In the presence of IB and PB with molar ratio of template : Co^{2+} = 0.3, dice-like particles generated at the lower concentration of IL (template : Co^{2+} = 0.2) transformed into rod-like particles which is shown in Figs. 4e and 4f, respectively. Figure S7e,f (ESI) reveals the higher magnified images of the corresponding samples. With further increase in molar ratio of template : Co^{2+} to 0.4, the rod-like morphology was obtained for all the samples prepared in the presence of CTAB (Fig. 4g), IB (Fig. 4h) and PB (Fig. 4i). However, CTAB-

assisted samples show a little bit aggregation in rod-like particles as compared to IB and PB-assisted samples; the microstructures are clearly observed from their higher magnified images of the corresponding samples (Fig. S7g-i, ESI). The morphology of the as-prepared $CoC_2O_4.xH_2O$ samples synthesized with molar ratio of template : Co^{2+} = 0.3 show a mixture of dice and rod-like particles in the presence of CTAB, and rod-like microstructure in the presence of IB and PB (Fig. S8a-c, ESI). It indicates that morphology remains unchanged through the transformation of $CoC_2O_4.xH_2O$ to Co_3O_4 after calcinations at 300^{o}C.

It is to be noted that the different cationic templates shows different morphologies. It is due to different chemical structures and the nature of interactions of the templates with the nuclei. In the presence of CTAB, self-assembly of the surfactants leads to the formation of micelles and bilayer structures.[60] There occurs seed-nuclei oriented attachment process via adsorption of colloids by sharing of a CTAB bilayer.[61] At lower concentration of CTAB, the growth of the particles becomes random due to metastability of the adsorbed colloid particles surrounded by CTAB bilayer. It renders flake or dice-like morphology. However, with increase in CTAB concentration, more and more CTAB bilayer is formed resulting preferential adsorption of more nuclei onto the seed particles, and the growth of the particles is oriented in 1D direction. It results rod-like morphology of the particles. It is worth mentioning that unlike long-chain alkylammonium surfactant (CTAB), the short chain IL (1-butyl-3-methylimidazolium bromide and pyridinium bromide) cannot preferentially self-assemble into micelle structure and bilayer aggregates through the rearrangement of the hydrophobic and hydrophilic molecular chains in solution. In case of IL, there occurs π- π stack interaction

and hydrogen bonding[62-64] of the neighbouring imidazolium, and pyridinium rings. The cationic parts of IL i.e., pyridinium and 1-butyl-3-methyl imidazolium ions are aligned and arrayed along seed layers, which is driven by coulomb coupling force with the Br^- ions. It favours in the formation of rod-like structure. However, at relatively lower concentration of IL, dice-like particles is formed instead. It demonstrates that an optimum concentration of IL is required for hydrogen bond-*co*-π-π interaction toward the formation of rod-like particles.

Figure 5a-i shows the TEM images (low and high magnified images) of the calcined (300^{o}C) samples prepared using CTAB, IB and PB, respectively, with template : Co^{2+} molar ratios of 0.2 (Fig. 5a, b, c), 0.3 (Fig. 5d, e, f) and 0.4 (Fig. 5g, h, i). For template : Co^{2+} molar ratio of 0.2, the flake-shape particles of CTAB-assisted samples, and dice-like particles in the presence of IB and PB are clearly noticed from TEM images. In the presence of IB and PB with template : Co^{2+} molar ratio of 0.3-0.4 each, and in the presence of CTAB with CTAB : Co^{2+} molar ratio of 0.4, the rod-like morphology (diameter of the rod ranges from 100-500 nm) of the particles was identified. However, with CTAB : Co^{2+} molar ratio of 0.3, the synthesized particles comprised of dice and rod-shape particles. The presence of interparticle pores and the pores generated within the interface of nanorod arrays are observed from TEM images. The pores were not uniform with a lack of particular sizes and shapes. The as-prepared $CoC_2O_4.xH_2O$ samples prepared with molar ratio of template : Co^{2+} = 0.3 also indicate the presence of dice and rod-like morphology with CTAB, and rod-like microstructure in the presence of IB and PB (Fig. S9a-c, ESI). The selected area electron diffraction (SAED) patterns (Fig. S10a-i, ESI) for the calcined (300^{o}C) samples prepared using CTAB, IB and PB,

respectively with template : Co^{2+} molar ratios of 0.2 (Fig. S10a,b,c, ESI), 0.3 (Fig. S10d,e.f, ESI) and 0.4 (Fig. S10g,h,i, ESI) corresponded to the cubic Co_3O_4 phase (also confirmed from XRD) with polycrystalline nature of the samples, which was further confirmed by the corresponding HRTEM images (Fig. S11a-i, ESI). The d-spacing of 0.24 nm, 0.28 nm and 0.46 nm corresponded to the lattice planes of (311), (220) and (111) cubic Co_3O_4, respectively.

Figure 6 shows the nitrogen adsorption-desorption isotherms of the calcined (300^oC) samples prepared using (a) CTAB, and (b) IB and (c) PB with molar ratio of template : Co^{2+} as (A) 0.2, (B) 0.3 and (C) 0.4. It displays type IV isotherm plots according to IUPAC classification, which indicated mesoporous characteristic of the sample. The curves show type H-3 hysteresis loop. It indicated that asymmetric, interconnected, slit-like mesoporosity existed in the samples. The BJH pore size distributions (PSDs) of the corresponding samples derived from adsorption data of the isotherms are shown in the insets of Figure 6. The PSD curves indicate the absence of regular shapes and sizes of the pores in the samples. During thermal decomposition of $CoC_2O_4.xH_2O$ to Co_3O_4, interparticles mesopores were generated[65] which could be originated from the mesoporous voids[66] between the nanocrystallites of Co_3O_4. Table S1 summarizes the textural properties of the samples (ESI). The BET surface area of CTAB-assisted samples decreased with increase in its relative molar concentration (with respect to Co^{2+}) from 0.2 to 0.3 followed by increasing the surface area value for relative molar concentration of 0.4. However, the BET surface area of IB and PB-assisted samples increased with increasing their relative molar concentration from 0.2 to 0.3 followed by lowering the surface area value for relative molar concentration of 0.4. It is noteworthy

that the morphology of the particles could play a significant role in changing the BET surface area values. The flake-like and rod-shape particles obtained in the presence of CTAB with 0.2 and 0.4 relative molar concentrations, respectively rendered higher surface area compared to that obtained with 0.3 relative molar concentration of CTAB, the latter exhibited rod-like particles along with dice-shape morphology. Due to the formation of dice-like particles obtained in the presence of IB and PB with the relative molar concentration of 0.2, the BET surface area values became lower. However, the rod-shape particles obtained in the presence of ionic liquid with the relative molar concentration of 0.3 significantly increased the BET surface area. The pore volume of all the samples ranged from 0.33 to 0.44 cc/g, while the pore size ranged from 19-53 nm.

Optical Absorption Study. To study the optical absorption characteristics and band gaps of the synthesized Co_3O_4 particles, the UV-VIS spectroscopy study was performed. The absorption spectra of the prepared Co_3O_4 show two peaks, at about 440 nm and 725 nm (Fig. S12a-i, ESI), which are due to ligand to metal charge transfer (LMCT). The former peak could be assigned to $O^{2-} \rightarrow Co^{2+}$, while the latter represents for $O^{2-} \rightarrow Co^{3+}$ LMCT.[67] Considering the absorption data, optical band gap was calculated using Tauc equation:

$$(\alpha h\nu)^n = K(h\nu - E_g) \qquad (3)$$

Where, α is absorption coefficient, hν is energy of photon, the value of n depends upon the material of the photocatalyst (n = 2 for direct allowed transition, n = 1/2 for indirect allowed transition, and n = 1/3 for indirect forbidden transition), in the present case n=2, E_g is band gap, and K is a constant.

Figure S13a-i (ESI) shows the plot of $(\alpha h\nu)^2$ versus hν. The band gap is calculated by extrapolating a tangent to x-axis. For Co_3O_4 semiconductor, two optical band gaps are obtained based on its band structure.[68] In Co_3O_4 semiconductor, the valence band (VB) possesses dominant O 2p character, where as 3d orbitals of Co^{2+} prevail in the conduction band (CB). The 3d orbitals of Co^{3+} remain as subband between the aforementioned VB and CB bands. The transition from VB to CB renders true band gap energy (E_{g2}), while E_{g1} is assigned to $O^{2-} \rightarrow Co^{3+}$ excitation. The values of E_{g1} and E_{g2} (Table S2, ESI) of Co_3O_4 photocatalysts with different morphologies are in the range of 1.4-1.5 eV and 1.5-1.9 eV, respectively. These values are comparable to those of reported Co_3O_4 semiconductors.[69]

Photocatalytic Degradation Study. Before irradiation of visible light, the adsorption ability (mg/g) of the samples to dye (kept in dark for 30 mins for homogenization) was studied. Figure S14 (ESI) shows the dye adsorption capacity (mg/g) for different samples. It reveals that the samples, CTAB-0.3, PB-0.2 and IB-0.2 having less surface area exhibited relatively lower adsorption capacity compared to that of the samples, IB-0.3, CTAB-0.4, PB-0.3, IB-0.4, CTAB-0.2, PB-0.4 having more surface area. In this case, the morphology of the samples has a little influence for dye adsorption. However, to study the affect of morphology as well as surface area of the samples, the photocatalytic activity of different shaped Co_3O_4 samples for the degradation of CSB in the presence of visible light was investigated. As the degradation of CSB proceeded, the characteristic absorption of CSB at λ_{max} = 618 nm gradually decreased. A blank (without using catalyst) experiment was performed for photocatalytic dye degradation to prove the photocatalytic performance of Co_3O_4. The degradation profile of CSB after

photocatalytic reaction with different Co_3O_4 catalyst prepared using CTAB, IB and PB with relative molar concentration (with respect to Co^{2+}) of 0.2, 0.3 and 0.4 are shown in Fig. S15, ESI. Figure 7A shows linear plot of $\ln(C_t/C_o)$ vs time, which confirmed pseudo-first order kinetics of the catalytic reactions. It is clear that dye concentration decreased with time, the rate of decrease of concentration in presence of Co_3O_4 catalyst prepared using different templates with various concentration followed as PB-0.3>IB-0.3>CTAB-0.4>IB-0.4>PB-0.4>PB-0.2>CTAB-0.3>IB-0.2>CTAB-0.2 with their rate constant values of 14.3×10^{-2} min^{-1}, 12.1×10^{-2} min^{-1}, 7.8×10^{-2} min^{-1}, 7.3×10^{-2} min^{-1}, 6.4×10^{-2} min^{-1}, 3.8×10^{-2} min^{-1}, 2.8×10^{-2} min^{-1}, 2.2×10^{-2} min^{-1}, and 2.2×10^{-2} min^{-1}, respectively. Fig. 7B represents a 3D plot exhibiting dependence of rate constant of photocatalytic azo-dye degradation on morphology and surface area of the photocatalyst. It is also shown in tabulated form (Table S3 in ESI). It reveals that the maximum rate constant i.e., the maximum photocatalytic efficiency (95% dye degradation) was obtained for rod-like particles having higher surface area (PB-0.3). Compared with previous results, the degradation rate of CSB using the synthesized rod-like Co_3O_4 photocatalysts (PB-0.3) having higher surface area was found to be maximum (Table S4 in ESI). Interestingly, unlike adsorption capacity (before irradiation of visible light), the degradation efficiency of different samples to dye in the presence of visible light has a significant affect on the morphology as well as surface area of the samples. The stability of catalytic efficiency was checked for 5 cycles with the catalyst, PB-0.3 which show maximum catalytic efficiency (Fig. 7C). It shows that catalytic activity remained practically the same as the original catalyst indicating recyclable of the catalyst.

It is interesting to point out that two properties i.e. morphology and surface area of the samples play the significant role for photocatalytic efficiency of Co_3O_4. The particles with rod-like morphology having higher surface area rendered higher catalytic efficiency. For PB-assisted Co_3O_4, the sample PB-0.3 with rod-shape morphology and highest surface area resulted maximum catalytic efficiency. However, the samples CTAB-0.2 having higher surface area than the samples, CTAB-0.3, CTAB-0.4, IB-0.2, IB-0.3, IB-0.4, PB-0.2, and PB-0.4 contributed least catalytic efficiency due to flake-like morphology of the former particles.

Mechanism of dye degradation. Initially the dye molecules are adsorbed on the surface of the photocatalyst. The well known mechanism of photoexcitation of the semiconductor photocatalyst on irradiation of light is involved. Schematic of the mechanism is shown in Fig 8. The photocatalyst on irradiation by light of suitable wavelength renders migration of electrons from valence band to conduction band through the band gap (E_g), generating electron deficit holes. Thus formation of electron-hole pairs occurs.[70] Generally, the photocatalytic reaction takes place at the surface of the photocatalyst. The electrons and highly oxidative holes present on the surface of the photocatalyst are trapped by oxygen and water, respectively, or by the surface adsorbed dye molecules. Thus a photocatalyst can allow facile migration of photogenarated charge carriers from the interior bulk to the surface, which is required to inhibit hole-electron recombination.[24,71] The nanosized channel walls in mesoporous photocatalyst facilitate faster electrons migration from bulk to the surface of photocatalyst.[72] Hence, mesoporous photocatalyst can successfully degrade water soluble organic pollutants by inhibiting recombination of photogenarated charge carriers. In VB, the holes are trapped by water molecules to form $^{\cdot}OH$ radicals. [73]

At the same time, the electrons in CB of Co_3O_4 semiconductor react with dissolved molecular oxygen present in water to produce superoxide radical anion $O_2^{\cdot -}$. This $O_2^{\cdot -}$ react with H_2O to furnish $^{\cdot}OH$ and $HOO^{\cdot}$ having powerful oxidizing ability.[74] On reacting with these powerful oxidizing agents, the dye gets oxidized and decolorized.[18] The furnished electron is able to regenerate the photocatalyst.

With increase in surface area of photocatalyst, the adsorption of dye as well as desorption process is facilitated. Mesoporous semiconductors of high surface area not only restrict recombination of photogenarated charge carriers, but they provide more surface reactive sites for photocatalytic dye degradation process. Interestingly, it is to be noted that the morphology of photocatalysts has a dominant role in reducing the recombination of electrons-holes pair, which influences the efficiency of photocatalyst. Photocatalyst with rod-like morphology exhibits better photocatalytic efficiency than flake-like morphology instead of having almost same surface area. It is reported that one-dimensional (1D) structures favour fast electron transport resulting in significant reduced recombination of the photogenerated charges.[75] Moreover the true band gap (E_{g2}) measurement depicts that the flake-like photocatalyst possess lower band gap than the rod-like photocatalyst. Thus the former shows lower photocatalytic efficiency.

Apart from morphology effect of samples, the band gap of the photocatalyst plays significant role in the increased photocatalytic efficiency, although having nearly same surface area. It can be inferred that mesoporosity, high surface area, 1D (rod-like) morphology of Co_3O_4 photocatalyst, and higher band gaps are responsible for rapid degradation of the model water soluble organic pollutant under visible light irradiation.

4. Conclusions

In summary, we have demonstrated the effect of cationic templates in tuning morphology and surface textural properties of Co_3O_4 toward excellent visible light photocatalytic efficiency for the degradation of Chicago Sky Blue 6B. The ionic liquids (1-butyl-3-methylimidazolium bromide and pyridinium bromide) generated rod-like structure (it is an ideal morphology to be attained by Co_3O_4 photocatalyst for faster reaction rate) more favourably than using CTAB due to the presence of π- π stack interaction and hydrogen bonding in the former. Among all the photocatalysts, PB-0.3 having rod-like morphology and highest surface area show maximum rate of photocatalytic dye degradation. This work provides a facile synthesis approach in tailoring morphology, textural properties and other physico-chemical behaviours by using various soft templates and ionic liquids for the synthesis of other metal oxides, which could be exploited for visible light photocatalysis applications.

Acknowledgement

The authors would like to thank the Director of this institute for his kind permission to publish this paper. The authors (M. Roy and S. Ghosh) are thankful to CSIR for their fellowship. The authors would like to thank Mr. Mritunjoy Maity and Mr. P. Anil Reddy for their help. The Nano-structured Materials Division is thankfully acknowledged for Raman spectra. The financial support from Department of Science and

Technology under DST-SERB sponsored project, GAP 0616 (Grant No.: SR/S3/ME/0035/2012), Government of India is thankfully acknowledged.

References

(1) M. Bruchez, J.M. Moronne, P. Gin, S. Weiss and A.P. Alivisatos, *Science*, 1998, 281, 2013-2016.

(2) D.S. Wang, T. Xie and Y.D. Li, *Nano Res.*, 2009, 2, 30-46.

(3) H.P. Cong and S.H. Yu, *Cryst. Growth Des.*, 2009, 9, 210-217.

(4) C. Zhao, B. Huang, J. Zhou and E. Xie, *Phys. Chem. Chem. Phys.*, 2014, 16, 19327-19332.

(5) W.Y. Li, L.-N. Xu, and J. Chen, *Adv. Funct. Mater.*, 2005, 15, 851-857.

(6) K. M. Shaju, F. Jiao, A. Débart and P. G. Bruce, *Phys. Chem. Chem. Phys.*, 2007, 9, 1837–1842.

(7) G. Wang, X. Shen, J. Horvat, B. Wang, H. Liu, D. Wexler and J. Yao, *J. Phys. Chem. C*, 2009, 113, 4357-4361.

(8) M. Yada, Y. Inoue, M. Koikawa, T. Torikai and T. Watari, *CrystEngComm*, 2012, 14, 7374-7381.

(9) T.-L. Lai, Y.-L. Lai, C.-C. Lee, Y.-Y. Shu and C.-B. Wang, *Catal. Today*, 2008, 131, 105-110.

(10) H. Sun, H. Ming Ang, M. O. Tade and S. Wang, *J. Mater. Chem. A*, 2013, 1, 14427-14442.

(11) X. Ke, J. Cao, M. Zheng, Y. Chen, J. Liu and G. Ji, *Mater. Lett.*, 2007, 61, 3901-3903.

(12) Y. Li, B. Tan and Y. Wu, *Nano Lett.*, 2008, 8, 265-270.

(13) X. W. Lou, D. Deng, J. Y. Lee, J. Feng and L. A. Archer, *Adv. Mater.*, 2008, 20, 258-262.

(14) Y. Wang, H. Xia, L. Lu and J. Lin, *ACS Nano*, 2010, 4, 1425-1432.

(15) M. Wang, L. Zeng and Q. Chen, *Dalton Trans.*, 2011, 40, 597-601.

(16) L. Chen, J. Hu, R. Richards, S. Prikhodko and S. Kodambaka, *Nanoscale*, 2010, 2, 1657-1660.

(17) X. Wang, H. Guan, S. Chen, H. Li, T. Zhai, D. Tang, Y. Bando and D. Golberg, *Chem. Commun.*, 2011, 47, 12280-12282.

(18) M. Roy, S. Ghosh and M. K. Naskar, *Dalton Trans.*, 2014, 43, 10248-10257.

(19) J. S. Chen, T. Zhu, Q.H. Hu, J. Gao, F. Su, S. Z. Qiao and X. W. Lou, ACS Appl. Mater. Interfaces, 2010, 2, 3628-3635.

(20) X. Xie, Y. Li, Z -Q. Liu, M. Haruta and W. Shen, *Nature*, 2009, 458, 746-749.

(21) C. Y. Ma, Z. Mu, J -J. Li, Y. G. Jin, J. Cheng, G. Q. Lu, Z. P. Hao and S. Z. Qio, *J. Am. Chem. Soc.,* 2010, 132, 2608-2613.

(22) H. G. Kim, P. H. Borse, W. Choi and J. S. Lee, *Angew. Chem., Int. Ed.*, 2005, 44, 4585-4589.

(23) Q. Jin, H. Yamamoto, K. Yamamoto, M. Fujishima and H. Tada, *Phys. Chem. Chem. Phys.*, 2013, 15, 20313–20319.

(24) H.-Y. Jiang, K. Cheng and J. Lin, *Phys. Chem. Chem. Phys.*, 2012, 14, 12114–12121.

(25) R. Georgekutty, M. K. Seery and S. C. Pillai *J. Phys. Chem. C*, *2008*, 112, 13563–13570.

(26) X. Gao, H. B. Wu, L. Zheng, Y. Zhong, Y. Hu and X. W. Lou, *Angew. Chem. Int. Ed.*, 2014, 53, 5917 –5921.

(27) Y. Jiao, Y. Liu, F. Qu and X. Wu, *CrystEngComm*, 2014, 16, 575-580.

(28) T. Warang, N. Patel, A. Santini, N. Bazzanella, A. Kale and A. Miotello, *Appl. Catal. A: General*, 2012, 423-424, 21-27.

(29) F. Li, D. E. Zhang and Z. W. Tong, *Synthesis and Reactivity in Inorganic, Metal-Organic, and Nano-Metal Chemistry*, 2013, 43, 756-760.

(30) X. Lou, J. Han, W. Chu, X. Wang and Q. Cheng, *Mater. Sci. Eng. B*, 2007, 137, 268-271.

(31) L. Pan, L. Li, D. Tian, C. Li and J. Wang, *JOM*, 2014, 66, 1035-1042.

(32) G. Wang, H. Liu, J. Horvat, B. Wang, S. Qiao, J. Park and H. Ahnidl, *Chem. - Eur. J.*, 2010, 16, 11020-11027.

(33) J. Deng, L. Zhang, H. Dai, Y. Xia, H. Jiang, H. Zhang and H. He, *J. Phys. Chem. C*, 2010, 114, 2694-2700.

(34) C. -A. Wang, S. Li and L. An, *Chem. Commun.*, 2013, 49, 7427-7429.

(35) N. Dahal, I. A. Ibarra and S. M. Humphrey, *J. Mater. Chem.*, 2012, 22, 12675-12681.

(36) J. Zheng, J. Liu, D. Lv, Q. Kuang, Z. Jiang, Z. Xie, R. Huang and L. Zheng, *J. Solid State Chem.*, 2010, 183, 600-605.

(37) F. Cao, D. Wang, R. Deng, J. Tang, S. Song, Y. Lei, S. Wang, S. Su, X. Yang and H. Zhang, *CrystEngComm*, 2011, 13, 2123-2129.

(38) B. Wang, T. Zhu, H. B. Wu, J. S. Chen and X. W. Lou, *Nanoscale*, 2012, 4, 2145-2149.

(39) T. Zhu, J. S. Chen and X. W. Lou, *J. Mater. Chem.*, 2010, 20, 7015-7020.

(40) R. Ranjan, S. Vaidya, P. Thaplyal, M. Qamar, J. Ahmed and A.K. Ganguli, *Langmuir*, 2009, 25, 6469-6475.

(41) L. Guo, H. Arafune and N. Teramae, *Langmuir*, 2013, 29, 4404-4412.

(42) S. Ghosh, M. Roy and M. K. Naskar, *Cryst. Growth. Des.*, 2014, 14, 2977-2984.

(43) D. Wang, Q. Wang and T. Wang, *Inorg. Chem.*, 2011, 50, 6482-6492.

(44) L. Ren, P. P. Wang, Y. S. Han, C. W. Hu and B. Q. Wei, *Chem. Phys. Lett.*, 2009, 476, 78-83.

(45) N. Du, Y. F. Xu, H. Zhang, C. X. Zhai and D. R.Yang, *Nanoscale Res. Lett.*, 2010, 5, 1295-1300.

(46) W. A. Ang, Y. L. Cheah, C. L. Wong, R. Prasanth, H. H. Hng and S. Madhavi, *J. Phys. Chem. C*, 2013, 117, 16316−16325.

(47) P. Wasserscheid and T. Welton, *Ionic Liquids in Synthesis*, 2nd ed.; Wiley-VCH: Weinheim, 2008.

(48) E.R. Parnham and R.E. Morris, *Acc. Chem. Res.*, 2007, 40, 1005-1013.

(49) T. Wang, H. Kaper, M. Antonietti and B. Smarsly, *Langmuir*, 2007, 23, 1489-1495.

(50) Y. Wang, K. Deng and L. Zhang, *J. Phys. Chem. C*, 2011, 115, 14300–14308.

(51) W. -W. Wang and Y. -J. Zhu, *Mater. Res. Bull.*, 2005, 40, 1929-1935.

(52) A. K. Mohammed and K. T. McKenzie, *J. Environ. Sci.*, 2005, 17, 869-872.

(53) J. Bacsa, D. Eve and K. R. Dunbar, *Acta Crystallogr., Sect. C: Cryst. Struct. Commun.*, 2005, C61, m58-m60.

(54) S. C. Petitto, E. M. Marsh, G. A. Carson and M. A. Langell, *J. Mol. Catal. A: Chem.*, 2008, 281, 49-58.

(55) L. Ren, P. P. Wang, Y. S. Han, C. W. Hu and B. Q. Wei, *Chem. Phys. Lett.*, 2009, 476, 78-83.

(56) H. -P. Cong and S. -H. Yu, *Cryst. Growth Des.*, 2009, 9, 210-217.

(57) T. E. Karis, X. -C. Guo, B. Marchon, V. Raman and Y. -L. Hsiao, *IEEE Trans. Magn.*, 2006, 42, 2507-2509.

(58) W. Song, C. Sun, W. Yin and Z. Men, *Optik*, 2014, 125, 6131-6135.

(59) C. W. Na, H. -S. Woo, H. -J. Kim, U. Jeong, J. -H. Chung and J.-H. Lee, *CrystEngComm*, 2012, 14, 3737-3741.

(60) H. Xu and W. Wang, *Angew Chem. Int. Ed.*, 2007, 46, 1489-1492.

(61) L. Bisson, C. Boissiere, L. Nicole, D. Grosso, J. P. Jolivet, C. Thomazeau, D. Uzio, G. Berhault and C. Sanchez, *Chem. Mater.*, 2009, 21, 2668-2678.

(62) T. Kim, J. Lian, J. Ma, X. Duan and W. Zheng, *Cryst. Growth Des.*, 2010, 10, 2928-2933.

(63) J. Lian, J. Ma, X. Duan, T. Kim, H. Li and W. Zheng, *Chem. Commun.*, 2010, 46, 2650-2652.

(64) H. Chen and S. Dong, *Langmuir*, 2007, 23, 12503-12507.

(65) B. Wang, H. B. Wu, L. Zhang, X. W. Lou, *Angew. Chem. Int. Ed.* 2013, 52, 4165-4168.

(66) J. H. Pan, Q. Huang, Z. Y. Koh, D. Neo, X. Z. Wang and Q. Wang, *ACS Appl. Mater. Interfaces,* 2013, 5, 6292-6299.

(67) D. Barreca, C. Massignan, S. Daolio, M. Fabrizio, C. Piccirillo, L. Armelao and E. Tondello, *Chem. Mater.*, 2001, 13, 588−593.

(68) S. Thota, A. Kumar, J. Kumar, *Mater. Sci. Eng. B*, 2009, 164, 30–37.

(69) S. A. Makhlouf, Z. H. Bakr, K. I. Aly and M.S. Moustafa, *Superlattices Microstruct.*, 2013, 64, 107–117.

(70) S. K. Kansal, M. Singh and D. Sud, *J. Hazard. Mater.*, 2007, 141, 581-590.

(71) J. Yu, Q. Li, S. Liu, and M. Jaroniec, *Chem. Eur. J.*, 2013, 19, 2433 – 2441.

(72) L. Guo, D. Jing, M. Liu, Y. Chen, S. Shen, J. Shiand and K. Zhang, *Beilstein J. Nanotechnol.*, 2014, 5, 994-1004.

(73) S.-H. Hsieh, G.-J. Lee, C.-Y. Chen, J.-H. Chen, S.-H. Ma, T.-L. Horng, K.-H. Chen and J. J. Wu, *Top. Catal.*, 2013, 56, 623-629.

(74) A. K. Kole, C. S. Tiwary and P. Kumbhakar, *CrystEngComm*, 2013, 15, 5515-5525.

(75) X. Bian, K. Hong, X. Ge, R. Song, L. Liu and M. Xu, *J. Phys. Chem. C*, 2015, 119, 1700−1705.

Figure Captions

Figure 1: XRD patterns of (A) as-prepared and (B) calcined samples synthesized using (a) CTAB, (b) IB and (c) PB with molar ratio of template : Co^{2+} as 0.3.

Figure 2: FTIR spectra of (A) as-prepared and (B) calcined samples synthesized using (a) CTAB, (b) IB and (c) PB with molar ratio of template : Co^{2+} as 0.3.

Figure 3: Raman spectra of (A) as-prepared and (B) calcined samples synthesized using (a) CTAB, (b) IB and (c) PB with molar ratio of template : Co^{2+} as 0.3.

Figure 4: FESEM micrographs of the calcined samples synthesized using CTAB, IB and PB with different concentrations: (a) CTAB-0.2, (b) IB-0.2, (c) PB-0.2, (d) CTAB-0.3, (e) IB-0.3, (f) PB-0.3, (g) CTAB-0.4, (h) IB-0.4, and (i) PB-0.4.

Figure 5: TEM images of the calcined samples synthesized using CTAB, IB and PB with different concentrations: (a) CTAB-0.2, (b) IB-0.2, (c) PB-0.2, (d) CTAB-0.3, (e) IB-0.3, (f) PB-0.3, (g) CTAB-0.4, (h) IB-0.4, and (i) PB-0.4.

Figure 6: N_2 adsorption-desorption isotherms of the calcined samples prepared using (a) CTAB, and (b) IB and (c) PB with molar ratio of template : Co^{2+} as (A) 0.2, (B) 0.3 and (C) 0.4. The insets show the corresponding pore size distribution curves.

Figure 7: (A) Plot of $\ln(C_t/C_o)$ vs.time for the degradation of Chicago sky blue 6B (CSB) dye without any catalyst (blank), with catalyst: (a) CTAB-0.2, (b) IB-0.2, (c) PB-0.2, (d) CTAB-0.3, (e) IB-0.3, (f) PB-0.3, (g) CTAB-0.4, (h) IB-0.4, and (i) PB-0.4, (B) Rate constant value of the photocatalysts as the function of surface area and morphology, and (C) Rate constant values for the same degradation in five consecutive cycles using the sample, PB-0.3.

Figure 8: Mechanism of photoexcitation and dye decomposition by semiconductor photocatalyst.

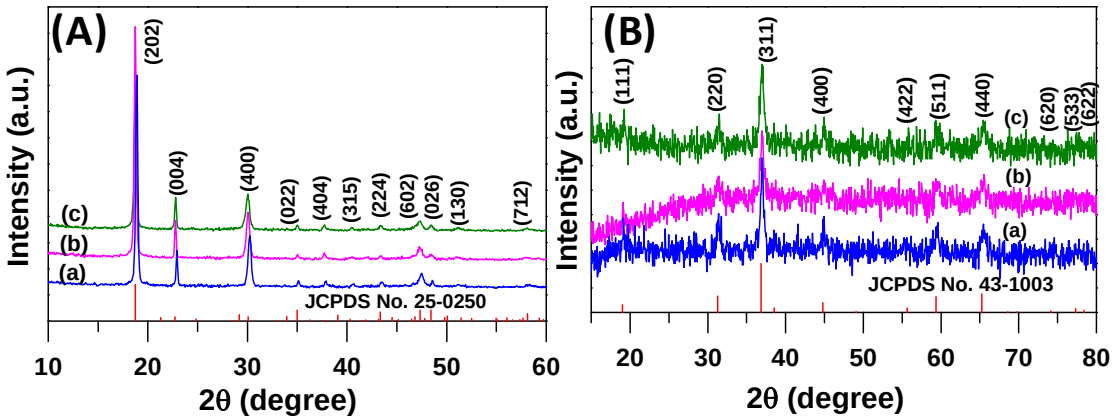

Figure 1: XRD patterns of (A) as-prepared and (B) calcined samples synthesized using (a) CTAB, (b) IB and (c) PB with molar ratio of template : Co^{2+} as 0.3.

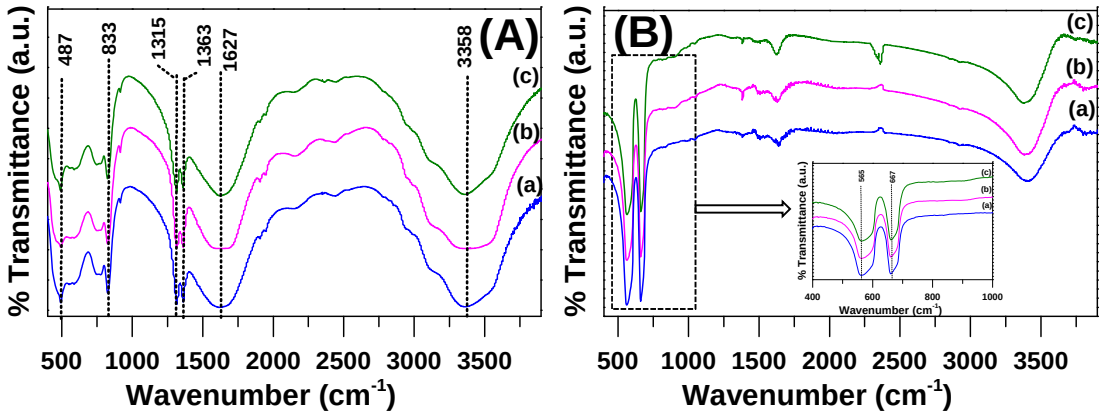

Figure 2: FTIR spectra of (A) as-prepared and (B) calcined samples synthesized using (a) CTAB, (b) IB and (c) PB with molar ratio of template : Co^{2+} as 0.3.

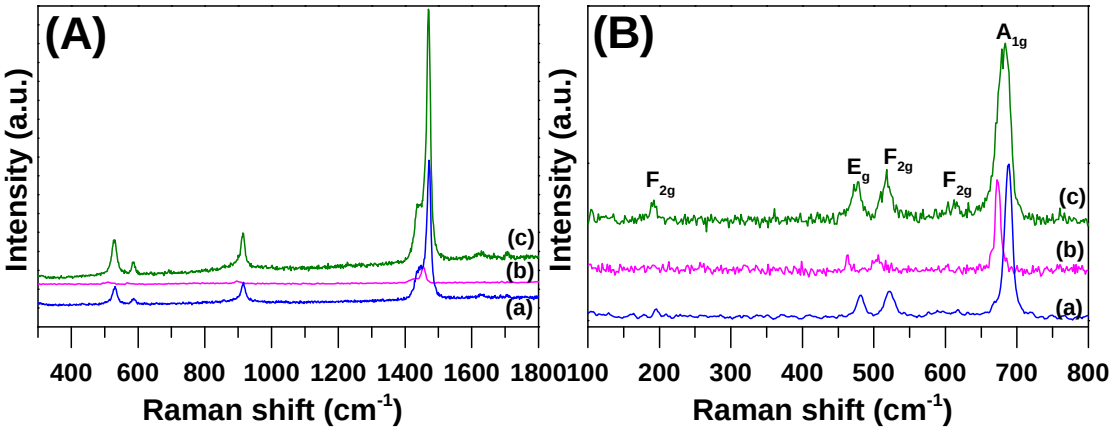

Figure 3: Raman spectra of (A) as-prepared and (B) calcined samples synthesized using (a) CTAB, (b) IB and (c) PB with molar ratio of template : Co^{2+} as 0.3.

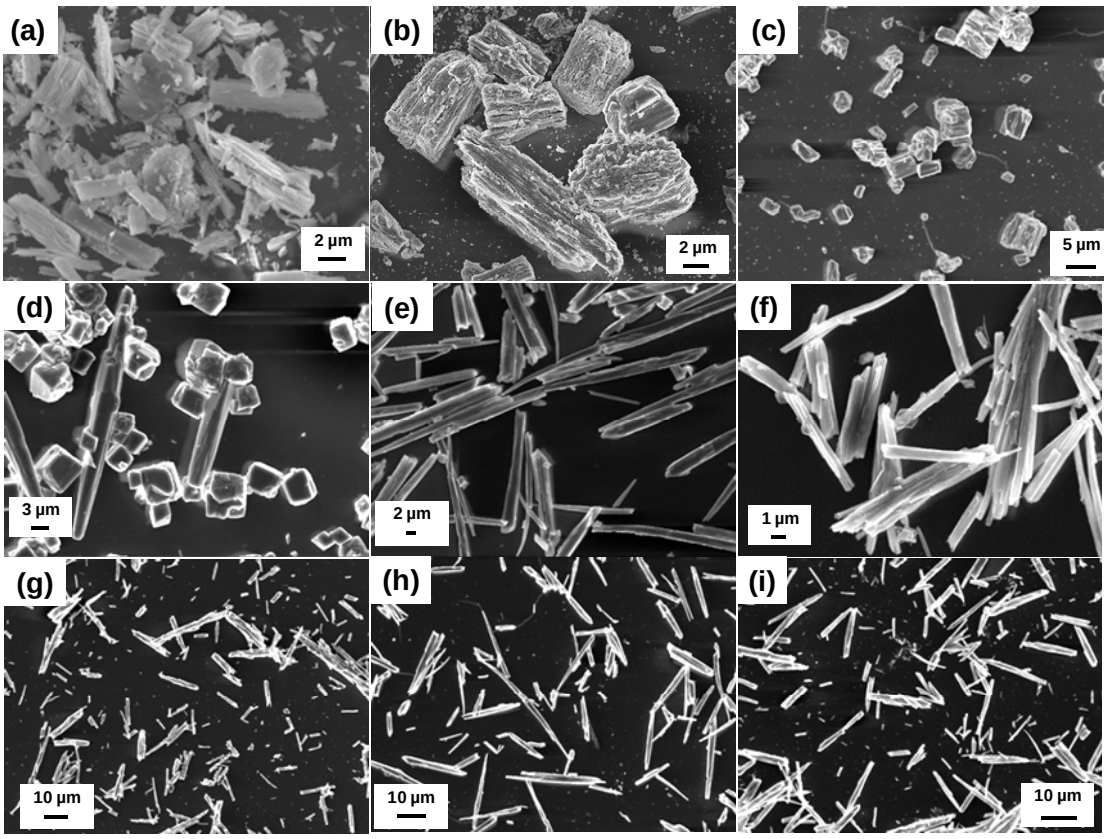

Figure 4: FESEM micrographs of the calcined samples synthesized using CTAB, IB and PB with different concentrations: (a) CTAB-0.2, (b) IB-0.2, (c) PB-0.2, (d) CTAB-0.3, (e) IB-0.3, (f) PB-0.3, (g) CTAB-0.4, (h) IB-0.4, and (i) PB-0.4.

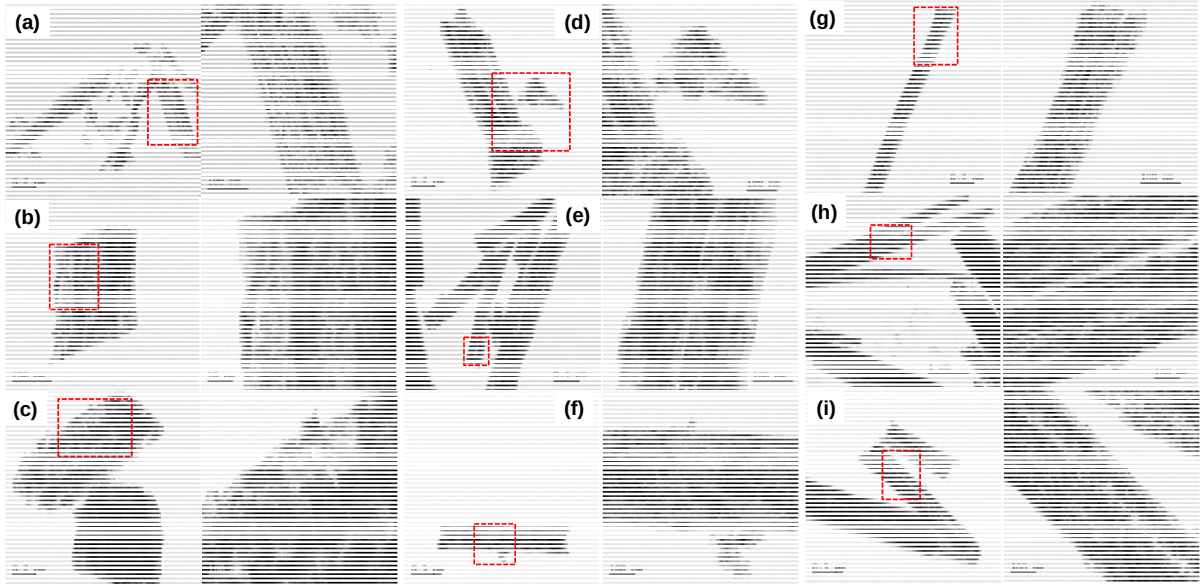

Figure 5: TEM images of the calcined samples synthesized using CTAB, IB and PB with different concentrations: (a) CTAB-0.2, (b) IB-0.2, (c) PB-0.2, (d) CTAB-0.3, (e) IB-0.3, (f) PB-0.3, (g) CTAB-0.4, (h) IB-0.4, and (i) PB-0.4.

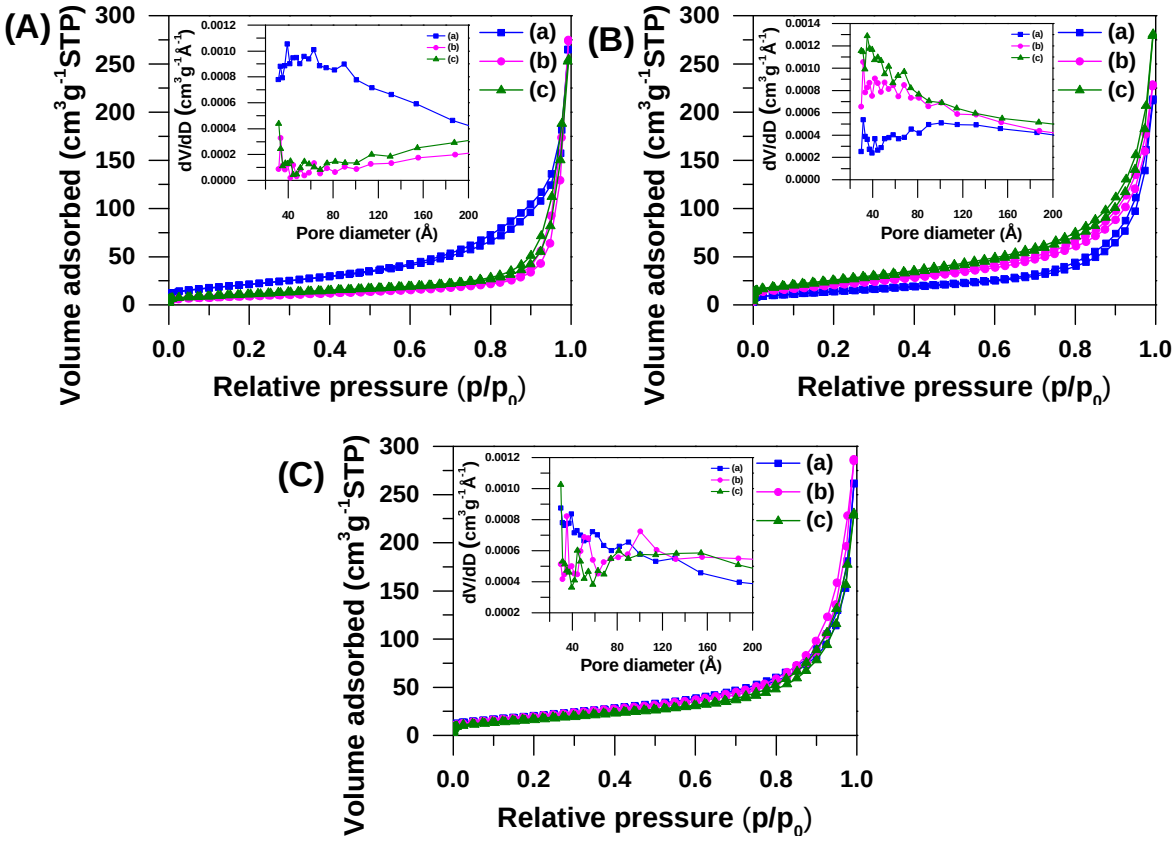

Figure 6: N_2 adsorption-desorption isotherms of the calcined samples prepared using (a) CTAB, and (b) IB and (c) PB with molar ratio of template : Co^{2+} as (A) 0.2, (B) 0.3 and (C) 0.4. The insets show the corresponding pore size distribution curves.

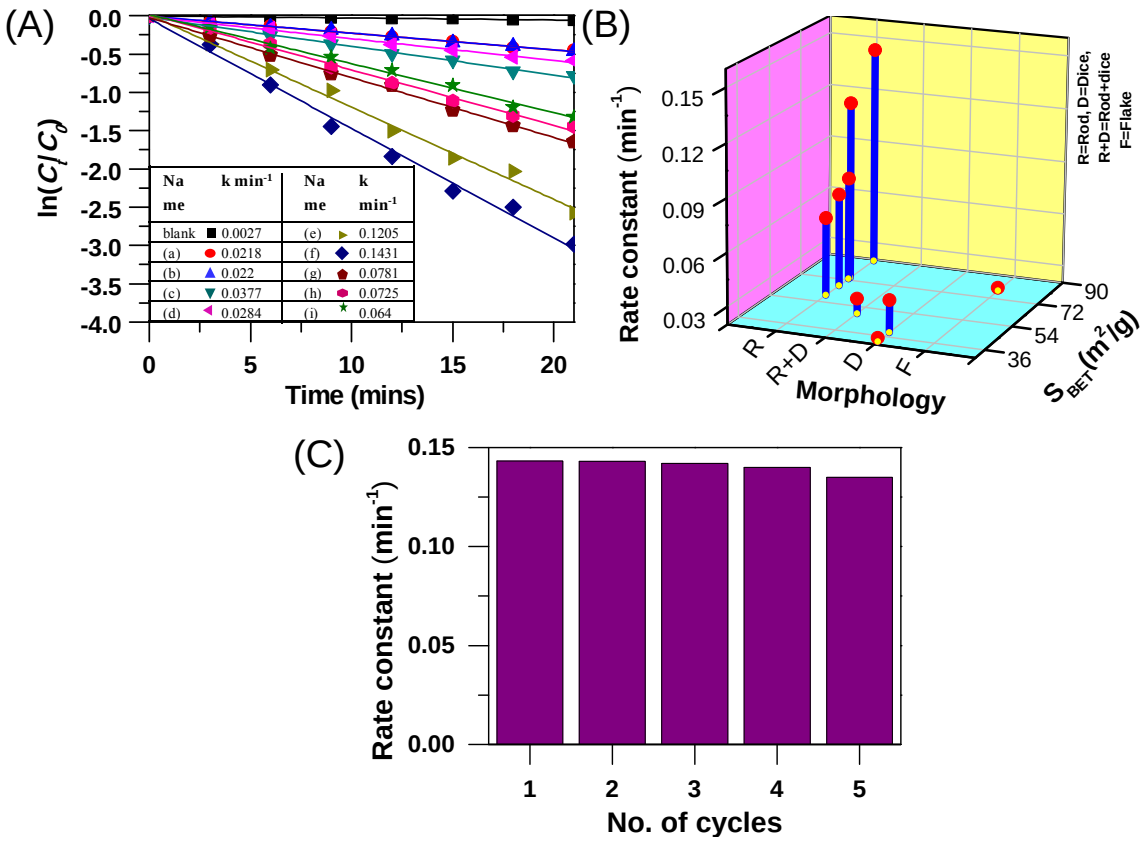

Figure 7: (A) Plot of $\ln(C_t/C_o)$ vs.time for the degradation of Chicago sky blue 6B (CSB) dye without any catalyst (blank), with catalyst: (a) CTAB-0.2, (b) IB-0.2, (c) PB-0.2, (d) CTAB-0.3, (e) IB-0.3, (f) PB-0.3, (g) CTAB-0.4, (h) IB-0.4, and (i) PB-0.4, (B) Rate constant value of the photocatalysts as the function of surface area and morphology, and (C) Rate constant values for the same degradation in five consecutive cycles using the sample, PB-0.3.

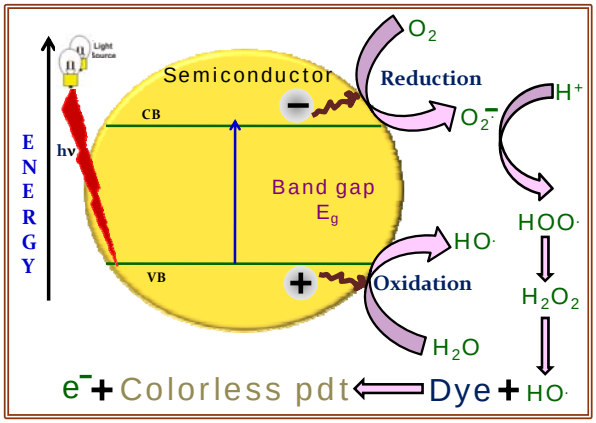

Figure 8: Mechanism of photoexcition and dye decomposition by semiconductor photocatalyst.

TOC Graphic

Ligand-assisted Soft-Chemical Synthesis of Self-assembled Shaped Mesoporous Co_3O_4: Efficient Visible Light Photocatalyst

Mouni Roy, Sourav Ghosh, and Milan Kanti Naskar*

Sol-Gel Division, CSIR-Central Glass and Ceramic Research Institute, Kolkata 700 032, India